Chapter 1
The Structure of Molecular Orbitals Investigated by Angle-Resolved Photoemission

Peter Puschnig, Georg Koller, Claudia Draxl, and Michael G. Ramsey

Abstract In this contribution, it is shown how the combination of angle-resolved photoemission spectroscopy (ARPES) with ab-initio electronic-structure calculations within the framework of density-functional theory (DFT) leads to insights into electronic and structural properties of organic molecular layers well beyond conventional density-of-sates or $E(k)$ investigations. In particular, we emphasize the rather simple, but for many cases sufficiently accurate, connection between the observed angular dependence of the photocurrent with the spatial distribution of the molecular orbital from which it is arising. After discussing the accuracy and limitations of this approach, which is based on a plane-wave approximation of the final state, three examples are presented. The first utilizes the characteristic angular pattern of the highest occupied molecular orbitals (HOMO) in a pentacene multilayer film in order to measure the molecular tilt angle in the film. In the second example, the nature of two closely spaced molecular emissions from a porphyrin thin film is unambiguously identified as HOMO and HOMO-1, and the molecule's azimuthal alignment is determined. Finally, for a monolayer of para-sexiphenyl on Cu(110), it is demonstrated how the real-space distribution of the filled LUMO and the HOMO of para-sexiphenyl can be reconstructed from the angular dependence of the photocurrent.

P. Puschnig (✉) · C. Draxl
Chair of Atomistic Modelling and Design of Materials, Montanuniversität Leoben, Franz-Josef-Straße 18, 8700 Leoben, Austria
e-mail: peter.puschnig@uni-graz.at

Present address:
P. Puschnig
Institute of Physics, Karl-Franzens University Graz, Universitätsplatz 5, 8010 Graz, Austria

Present address:
C. Draxl
Physics Department, Humboldt Universität zu Berlin, Zum Großen Windkanal 6, 12489 Berlin, Germany

G. Koller · M.G. Ramsey
Institute of Physics, Karl-Franzens University Graz, Universitätsplatz 5, 8010 Graz, Austria

1.1 Introduction

Electronic orbitals are the prime determinants of the respective compounds' chemical, electronic, and optical properties. Therefore, the knowledge of energetic positions, ordering, and spatial extent of molecular orbitals is of great interest. However, the valence bands of large conjugated molecules consist of a multitude of closely spaced molecular states, which makes their correct assignment challenging both experimentally and theoretically.

Experimentally, energy positions of molecular orbitals in organic molecular layers can be studied by ultra-violet photoemission spectroscopy (UPS) [1] or by scanning tunneling spectroscopy (STS) [2–7]. UPS has the advantage that accessible binding energies are not limited to a few electron volts from the Fermi level as in STS. However, UPS spectra of thin molecular layers on metals often show only weak and rather broad features and are, therefore, not always conclusive. Also, UPS data depend on the experimental geometry, molecular orientation, and photon energy, which further complicates the assignment of the measured peaks. Moreover, experimental techniques which are probing the *spatial* structure of individual orbitals are rare, and the interpretation of experimental data is commonly difficult and requires guidance from theory [8]. Here, scanning tunneling microscopy (STM) has proven to be a powerful technique for mapping orbital structures of rather complex molecules [2]. However, strong bonding interactions with the substrate make the interpretation of the images in terms of orbital structures problematic [9].

Angle-resolved photoelectron spectroscopy (ARPES), on the other hand, is *the* technique to study the band structure of solids by measuring the kinetic energy of the photoemitted electrons versus their angular distribution [10]. Particularly, many questions in nanophysics and interface engineering are often addressed by this experimental technique which, in combination with density-functional-theory calculations, leads to important physical insight. Recently, however, it has been shown that ARPES provides an alternative route to obtain information regarding the spatial structure of individual molecular orbitals [11–14]. By making certain assumptions about the photoemisson transition matrix element, ARPES intensity maps can also provide useful information regarding orbital structures. Specifically, it has become possible to obtain the one-dimensional wave functions of quantum-well states on nano-structured gold surfaces [13, 15], and the two-dimensional spatial electron distribution in the frontier orbitals of organic π-conjugated molecules adsorbed at metallic surfaces [12, 14].

In this contribution, we review the recent progress in measuring the spatial structure of molecular orbitals by using angle-resolved photoemission spectroscopy. By comparing measured ARPES data with simulations of the photoemission intensity based on density-functional theory, we demonstrate the strength of this method which lies in the direct and easy-to-apply connection between the measured angular dependence of the photocurrent and the Fourier transform of the molecular orbital from which electrons are emitted. First, we will give a brief account on the theoretical description which is based on the one-step model of photoemission. The implication of using a plane wave for the final state will be shown, and the limits of this approximation will be discussed. Then, three examples for molecular

films consisting of highly oriented multi-layers of π-conjugated molecules down to monolayers adsorbed at metallic surfaces will be given: First, results for a pentacene multilayer film are shown for which the tilt angle of the molecules could be determined from a comparison between the ARPES data and momentum maps of the free molecule. Second, data for a monolayer of tetraphenyl porphyrine on Cu(110) demonstrate the strength of the method in identifying of molecular orbitals and determining azimuthal molecular orientations. Finally, for a monolayer of para-sexiphenyl on Cu(110) it is demonstrated how ARPES momentum maps of the former lowest unoccupied molecular orbital (LUMO) and the highest occupied molecular orbital (HOMO) are utilized to reconstruct real-space distributions of the respective orbitals.

1.2 Theory

Photoemission spectroscopy is commonly applied to study the band structure of solids by measuring the kinetic energy versus angular distribution of the photoemitted electrons. Here we show that this experimental technique can also be used to gain information on the spatial electron distribution in molecular orbitals [12]. In angle-resolved photoemission spectroscopy (ARPES), schematically depicted in Fig. 1.1, an incident photon of energy $\hbar\omega$ excites an electron from a bound initial state, described by wave function ψ_i and energy E_i, to a final electron state ψ_f with kinetic energy E_{kin}. Because energy and momentum parallel to the surface are conserved during the photoemission process, the measurement of the emitted electron's energy and momentum probes the band structure of solids. Thus, ARPES is commonly used to study band dispersions, Fermi surfaces and many-body correlations in a wide range of materials [16].

1.2.1 One-Step Model of Photoemission

A theoretical description of the angle-resolved photoelectron intensity is generally rather involved, and attempts to compute it in a quantitative manner are rather scarce. Within this work, photo-excitation is treated as a single coherent process from a molecular orbital to the final state which is referred to as the one-step model of photoemission (PE). The PE intensity $I(\theta, \phi; E_{kin})$ is given by a Fermi golden rule formula [17]

$$I(\theta, \phi; E_{kin}) \propto \sum_i \left|\langle \psi_f(\theta, \phi; E_{kin})|\mathbf{A} \cdot \mathbf{p}|\psi_i\rangle\right|^2 \times \delta(E_i + \Phi + E_{kin} - \hbar\omega). \quad (1.1)$$

Here, the polar and azimuthal emission angles defined in Fig. 1.1 are denoted by θ and ϕ, respectively. The photocurrent I is given by a sum over all transitions from occupied initial states i described by wave functions ψ_i to the final state ψ_f

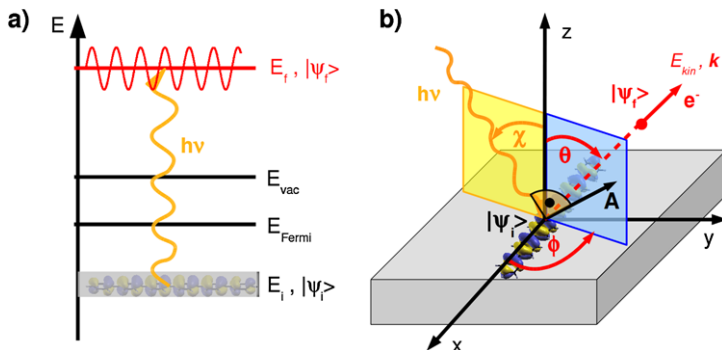**Fig. 1.1** (**a**) Schematic energy level diagram of a photoemission experiment showing the energy of the initial state, E_i, the Fermi level E_F, the vacuum level E_{vac}, and the final-state energy E_f. (**b**) In angle-resolved photoemission spectroscopy, an incident photon with energy $h\nu$ and vector potential $\mathbf{A}$ excites an electron from the initial state ψ_i to the final state ψ_f characterized by the kinetic energy E_{kin} and the momentum vector $\mathbf{k}$. The polar and azimuthal angles θ and ϕ, respectively, define the direction of the photoemitted electron

characterized by the direction (θ, ϕ) and the kinetic energy of the emitted electron. The delta function ensures energy conservation, where Φ denotes the sample work function. The transition matrix element is given in the dipole approximation, where $\mathbf{p}$ and $\mathbf{A}$, respectively, denote the momentum operator and the vector potential of the exciting electro-magnetic wave.

Plane-Wave Approximation

The difficult part in evaluating Eq. (1.1) is the proper treatment of the final state. In the most simple approach, it is approximated by a plane wave (PW) only characterized by the direction and wave number of the emitted electron. This has already been proposed more than 30 years ago [18] with some success in explaining the observed PE distribution from atoms and small molecules adsorbed at surfaces. Using a plane-wave approximation is appealing since the evaluation of Eq. (1.1) renders the photocurrent I_i arising from one particular initial state i proportional to the Fourier transform $\tilde{\psi}_i(\mathbf{k})$ of the initial-state wave function corrected by the polarization factor $\mathbf{A} \cdot \mathbf{k}$:

$$\left|\tilde{\psi}_i(\mathbf{k})\right| \propto \frac{\sqrt{I_i(\theta, \phi)}}{|\mathbf{A} \cdot \mathbf{k}|}. \tag{1.2}$$

Thus, if the angle-dependent photocurrent of individual initial states can be selectively measured (as it can for organic molecules where the intermolecular band dispersion is often smaller than the energetic separation of individual orbitals), a one-to-one relation between the photocurrent and the molecular orbitals in reciprocal space can be established. This allows the measurement of the absolute value

of the initial-state wave function in reciprocal space and, via a subsequent Fourier transform, a reconstruction of molecular orbital densities in real space.

Limitations of the Plane-Wave Approximation

It has been observed rather early that the plane-wave final-state approximation had problems in describing the photoemission intensity of some large polyatomic molecules and/or certain experimental geometries [19, 20]. This led to the conclusion that the plane-wave final-state approximation should not be used and nourished the development of the so-called independent-atomic-center (IAC) approximation [21]. In the IAC approximation, the initial state is decomposed into atomic eigenfunctions which build up the initial molecular orbitals, while the final state is composed of scattering solutions of the atomic Schrödinger equation at the final-state energy $E_k = \frac{\hbar^2}{2m}k^2$. The transition matrix element is then given by a coherent sum over these initial and final states, respectively. Thus, the IAC expression for the photoelectron wave function A with kinetic energy E_{kin} at the detector position $\mathbf{R}$ can be written in the following form [21]:

$$A(\mathbf{R}, E_{\text{kin}}) = \sum_{\alpha} \sum_{nlm} C_{\alpha,nlm} e^{i\mathbf{k}\mathbf{R}_\alpha} \sum_{LM} M^{LM}_{\alpha,nlm}(E_{\text{kin}}) Y_{LM}(\hat{R}). \qquad (1.3)$$

Here, the initial orbital $\psi_i(\mathbf{r})$ is expressed as a linear combination of atomic orbitals $\phi_{\alpha,nlm}$ centered at the position $\mathbf{R}_\alpha$, where nlm represent the principal and angular-momentum quantum numbers of the orbital and α the atomic center on which it resides:

$$\psi(\mathbf{r}) = \sum_{\alpha} \sum_{nlm} C_{\alpha,nlm} \phi_{\alpha,nlm}(\mathbf{r} - \mathbf{R}_\alpha). \qquad (1.4)$$

The matrix elements $M^{LM}_{\alpha,nlm}$ in Eq. (1.3) are dipole matrix elements between the atomic wave functions $\phi_{\alpha,nlm}$ and solutions of the Schrödinger equation in an atomic potential at the energy E_{kin} and angular momentum LM.

The goal of the remaining part of this section is to shed light on the relation between the IAC and the simpler PW approach and to hint towards possible limitations of the latter. It was already noted by Grobman that expression (1.3) can be considerably simplified if the initial molecular orbital is comprised of atomic orbitals of the same chemical and orbital character. A specific example of such a situation is given by a π molecular orbital of a planar polyatomic molecule. Then the coefficients $C_{\alpha,nlm}$ are only non-zero for atomic p_z orbitals and only one term remains of the sum over nlm:

$$A(\mathbf{R}, E_{\text{kin}}) = \sum_{\alpha} C_{\alpha,2p_z} e^{i\mathbf{k}\mathbf{R}_\alpha} \sum_{LM} M^{LM}_{2p_z}(E_{\text{kin}}) Y_{LM}(\hat{R}). \qquad (1.5)$$

In the above expression we have also omitted the atomic index α in the transition matrix elements since they do not depend on the position of the atom but only on the

type of atomic orbital which is assumed to be $2p_z$ for all contributing atoms. Thus, the sum over the final-state angular-momentum quantum numbers LM, the atomic factor, which we abbreviate as

$$N_{2p_z}(E_{\text{kin}}, \hat{R}) = \sum_{LM} M_{2p_z}^{LM}(E_{\text{kin}})Y_{LM}(\hat{R}), \tag{1.6}$$

can be put in front of the summation over atoms α and we are left with the simplified expression for the photoemission amplitude at the detector:

$$A(\mathbf{R}, E_{\text{kin}}) = N_{2p_z}(E_{\text{kin}}, \hat{R}) \sum_{\alpha} C_{\alpha,2p_z} e^{i\mathbf{k}\mathbf{R}_\alpha}. \tag{1.7}$$

As has been noted by Grobman [21] the term $N_{2p_z}(E_{\text{kin}}, \hat{R})$ acts only as a weakly varying envelope function while the main angular dependence of the photoemission intensity is dominated by the last term in Eq. (1.7), which is closely related to the Fourier transform of the initial molecular orbital. By taking the Fourier transform (FT) on both sides of Eq. (1.4) we see that the FT of the initial molecular orbital $\tilde{\psi}(\mathbf{k})$ can be written as

$$\tilde{\psi}(\mathbf{k}) = \tilde{\phi}_{2p_z}(\mathbf{k}) \sum_{\alpha} C_{\alpha,2p_z} e^{i\mathbf{k}\mathbf{R}_\alpha}. \tag{1.8}$$

Here, we have introduced the FT of a p_z orbital, $\tilde{\phi}_{2p_z}(\mathbf{k})$, whose angular part is simply given by the spherical harmonic, $Y_{10}(\theta, \phi) \propto \cos\theta$ [18].

Equivalence of IAC and PW Approximation

For large π conjugated molecules, the main angular dependence will be determined by the last term in Eq. (1.7). By combining Eqs. (1.7) and (1.8) we see that the IAC produces a result which is in fact very similar to the PW final-state assumption, compare Eq. (1.2), provided that the initial molecular orbital is composed of atomic orbitals of the same type as is the case for planar π conjugated molecules:

$$A(\mathbf{R}, E_{\text{kin}}) = \left(\frac{N_{2p_z}(E_{\text{kin}}, \hat{R})}{\tilde{\phi}_{2p_z}(\mathbf{k})} \right) \times \tilde{\psi}(\mathbf{k}). \tag{1.9}$$

Last but not least we note that the prefactor, $N_{2p_z}/\tilde{\psi}_{2p_z}$ can be shown to become completely independent of the emission direction (θ, ϕ) for the special case where the polarization vector $\mathbf{A}$ of the photon is exactly parallel to the emission direction $\mathbf{k}$. For this particular geometry the photoemission intensity resulting from the IAC, which is the square of $A(\mathbf{R}, E_{\text{kin}})$, reduces exactly to the intensity emerging from the plane-wave final-state assumption. This observation has already been made by Goldberg for the photoemission cross section from atoms [22]. Moreover, due to the overall weak angular dependence of the envelope factor $N_{2p_z}/\tilde{\psi}_{2p_z}$, the Fourier

transform of the initial molecular orbital $\tilde{\psi}(\mathbf{k})$ continues to provide a good description of the angle-dependent PE intensity also when the direction of the polarization vector deviates from the emission direction. Hence it is expected that the difference between the PW result, Eq. (1.2), and the IAC expression, Eq. (1.8), only grows weakly with the deviation from the above mentioned condition.

Summary of Theoretical Consideration

From what was said above, the plane-wave final-state assumption can be expected to be valid if the following conditions are fulfilled: (i) π orbital emissions from large planar molecules, (ii) an experimental geometry in which the angle between the polarization vector $\mathbf{A}$ and the direction of the emitted electron $\mathbf{k}$ is rather small, and (iii) molecules consisting of many light atoms (H, C, N, O). The latter requirement is a result of the small scattering cross section of light atoms and the presence of many scattering centers expected to lead to a rather weak and structureless angular pattern [11, 23]. With these conditions satisfied, a one-to-one mapping between the PE intensity and individual molecular orbitals in reciprocal space is possible, providing a valuable tool for the investigation of organic molecular films and monolayers. This will be demonstrated with several examples in the following sections.

1.3 Photoemission Experiments

Presently, there are a number of display-type analyzers that are capable of obtaining angular-dependent photoemission intensity maps suitable for our approach [24]. Our ARPES experiments are performed at room temperature using a toroidal electron-energy analyzer described elsewhere [25] attached to the TGM-4 beamline at the synchrotron radiation facility BESSY II. This toroidal electron analyzer allows simultaneous collection of photoelectrons in a kinetic energy window of 0.8 eV over a polar angle θ range of 180° in the specular plane. Azimuthal scans are then made by rotating the sample around the surface normal in 1° steps for $>$180° of azimuthal angle ϕ. The angular emission data are then converted to momentum $k_{\parallel}$ using the formula $k_{\parallel} = \sqrt{2m_e E_{\mathrm{kin}}/\hbar^2}\sin\theta$ [Å^{-1}] to create the momentum maps. The photon incidence angle is $\alpha = 40°$, and the polarization direction is always in the specular plane. A photon energy of $h\nu = 35$ eV is used throughout.

1.4 Results

In this section, we demonstrate the viability of the simple plane-wave final-state approach in conjunction with initial-state orbitals taken from density-functional theory for a number π-conjugated organic molecules. First, we present data for the
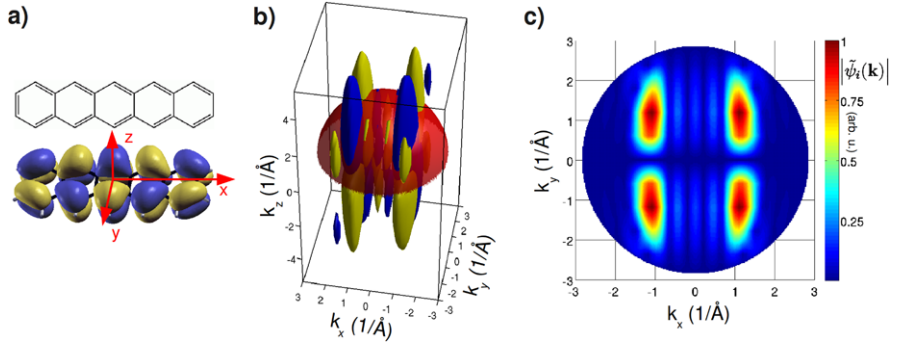
Fig. 1.2 (**a**) Chemical structure of pentacene and its highest molecular orbital (HOMO) calculated from density-functional theory. (**b**) Three-dimensional Fourier transform of the pentacene HOMO orbital, *yellow* (*blue*) showing an isosurface of a constant positive (negative) value. The *red hemisphere* illustrates a region of constant kinetic energy as explained in the text. (**c**) Absolute value of the pentacene HOMO Fourier transform on the hemisphere indicated in panel (**b**)

well-known molecular semiconductor pentacene in a multilayer thin film. Here, we focus on the emission from the HOMO and show that ARPES momentum maps—when compared to calculations—allow for a precise determination of the molecular tilt angle. As a second example, we compare ARPES momentum maps of a monolayer of tetraphenyl porphyrine with calculations of the PE intensity allowing for an identification of the HOMO and HOMO-1 and the determination of the azimuthal molecular orientation. Thirdly, we demonstrate that in certain cases the PW final-state approach enables a reconstruction of real-space orbitals. Here, we show ARPES data of a monolayer of para-sexiphenyl bonded to the Cu(110) surface. Not only are we able to reconstruct a real-space image of the HOMO but we also show that the PE intensity at the Fermi level that appears on adsorption has the orbital structure of the lowest unoccupied molecular orbital (LUMO).

1.4.1 Determination of Molecular Orientations

Pentacene is a planar aromatic molecule consisting of five linearly edge-fused phenyl rings, and has been extensively studied due to its interesting opto-electronic properties. Its electronic structure, in particular the intermolecular HOMO dispersion, has been analyzed by means of both photoemission experiments [26–28] and calculations within the framework of density-functional theory [29–31].

To illustrate the relation between the measured PE intensity and the FT of the emitting orbital, we calculate the electronic structure of an isolated pentacene molecule using DFT [32]. The resulting HOMO orbital is depicted in Fig. 1.2a, and its corresponding three-dimensional FT in Fig. 1.2b. Because the momentum maps are measured at constant binding energy, we evaluate the FT on a hemisphere of radius $k = \sqrt{(2m/\hbar^2)E_{\text{kin}}}$ (indicated in red). The value of the FT on that hemisphere
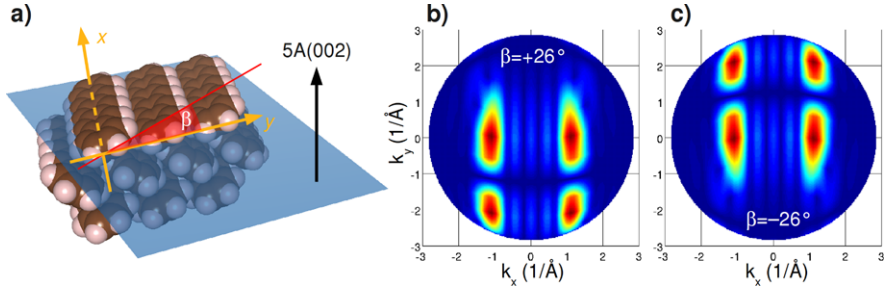
Fig. 1.3 (**a**) Geometry of the (002) plane of pentacene crystal structure exhibiting flat lying molecules with a tilt angle of $\beta = 26°$. (**b**) Simulated Fourier transform of the pentacene HOMO of a molecule with a tilt angle of $\beta = 26°$. (**c**) Same as (**b**) but for a tilt angle of $\beta = -26°$

for a kinetic energy of 29.8 eV is shown in Fig. 1.2c. We observe four main intensity maxima centered around $(k_x = 1.15, k_y = 1.2)$ Å^{-1} and symmetrically located around the Γ point (normal emission). For emission planes parallel (perpendicular) to the long (short) molecular axis, i.e., in the xz and yz planes, respectively, a vanishing photoemission intensity is predicted. This fact is reflecting the nodal structure of the pentacene HOMO orbital.

When the molecule is vacuum deposited on the p(2x1) oxygen reconstructed Cu(110) surface, its long axis orients parallel to the oxygen rows, resulting in crystalline pentacene(022) films [33] as depicted in Fig. 1.3a. When comparing the theoretical results of Fig. 1.2 with the experimental ARPES data of a multilayer of pentacene grown on a Cu(110)-(2x1)O substrate, one has to consider the orientation of the molecules in this multilayer film. From X-ray diffraction pole-figure measurements [33], the contact plane is determined to be the (022) crystallite orientation. As visualized in Fig. 1.3, this surface termination exhibits molecules with their long axis parallel to the surface but the π face tilted out of the surface plane by an angle of $\beta = 26°$. When this tilt angle is taken into account in the calculation of the Fourier transform, the four main lobes described above are shifted in y direction. This is illustrated in Figs. 1.3b and c, which show the pentacene HOMO of a molecule with a tilt angle of $\beta = 26°$ and $\beta = -26°$, respectively.

In the multilayer film, an effective average of the two molecular orientations, $+26°$ and $-26°$, is to be expected due to the two-fold symmetry of the substrate surface. In Fig. 1.4, we therefore compute an average of the results for $\beta = 26°$ and $\beta = -26°$. Figure 1.4 also shows an experimental momentum map, at the HOMO energy of a pentacene multilayer using a toroidal electron-energy analyzer at the synchrotron radiation facility BESSY II [25]. As a function of the momentum vector parallel to the molecular axis, k_x, there is a pronounced intensity maximum of the photoemission intensity centered at 1.15 Å^{-1}, as observed previously [28]. In the momentum maps, we see that these intense features extend about ± 0.8 Å^{-1} in k_y direction, and, in addition, there are weaker intensity lobes at about the same k_x value around $k_y \approx \pm 2$ Å^{-1}. The comparison between the simulated momentum map (Fig. 1.4a) and the measurement (Fig. 1.4b) is very satisfying. In particular, the

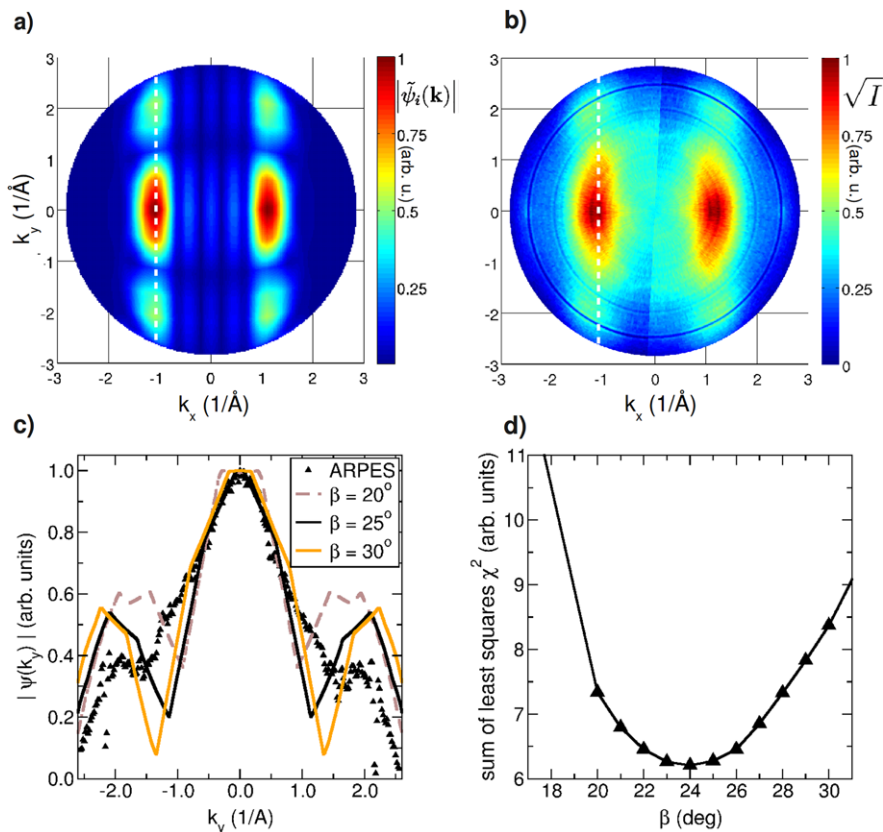**Fig. 1.4** (**a**) The sum of the data shown in Figs. 1.3b and c corresponding to the experimental situation where both tilts will be present. (**b**) Experimental photoemission intensity at a constant binding energy corresponding to the pentacene HOMO from the multilayer of pentacene as described in the text. (**c**) Experimental (*symbols*) vs. theoretical (*lines*) line scans at $k_x = -1.1$ Å as indicated by the *white dashed line* in (**a**) and (**b**). Simulations for three different tilt angles β are shown, $20°$ (*brown, dashed*), $25°$ (*black, solid*), $30°$ (*orange*). (**d**) Difference between experiment and simulation expressed as the sum of squared differences versus pentacene tilt angle β

maxima at the $k_y = 0$ line are clearly found to originate from the tilt angle of the molecules. Both the strong maxima at $k_y = 0$ and the weak peaks at $k_y = 2$ Å^{-1} result from the out-of-plane tilt angle of the pentacene molecules. Clearly, the FT approach describes the PE intensity well and therefore allows molecular orientations to be determined.

In order to emphasize the sensitivity of the PE intensity on the tilt angle we show a line scan along k_y at constant $k_x = -1.1$ Å as indicated by the white dashed line in Fig. 1.4a. These plots are shown in Fig. 1.4c where we compare the experimental line scan (symbols) with our simulated PE intensity for three different tilt angles β of the pentacene molecule. Clearly, the simulation result for $\beta = 25°$ is in better agree-

ment with the measurement than the computations for 20° and 30°, respectively. In particular, the peak position of the maxima around $k_y \approx \pm 2$ Å^{-1} are shifted to lower (higher) values by decreasing (increasing) the tilt angle. But also the shape of the main feature centered around $k_y = 0$ is reproduced better by the simulation for $\beta = 25°$. To quantify the quality of the simulations for various tilt angles β we also show the sum of the squared differences between the experimental line scans and the simulated ones in Fig. 1.4d. The curve shows a minimum at $\beta = 24°$ which is very close to the value of 26° obtained from X-ray pole-figure measurements on these pentacene multilayer films [33] and assuming the bulk structure from Mattheus and co-workers [34]. Thus, we estimate the accuracy of the ARPES approach to determine molecular tilt angles better than 5°. Compared to alternative methods, such as NEXAFS, the ARPES approach has the added advantage that rather than giving an average orientation, multiple orientations are immediately apparent and can be resolved. Moreover, ARPES works at low photon energies, minimizing damage to the sample, and does not require a tunable photon source.

1.4.2 Identification of Molecular Orbitals

In this section, it is demonstrated how ARPES momentum maps can be utilized to identify molecular states of organic molecules adsorbed on metallic surfaces beyond a simple comparison of calculated orbital energies with energy-distribution curves measured by UPS. As an example, we choose porphyrines which are of interest as versatile materials for organic electronics due to their tendency to form π–π stacked layers. In particular, thin films of tetraphenyl porphyrin, $C_{44}H_{30}N_4$, (H$_2$TPP) deposited on the oxygen reconstructed Cu(110)-(2x1)O surface have been shown to produce well-ordered, epitaxially aligned porphyrin thin films [35].

As can be seen from Fig. 1.5a, H$_2$TPP molecules consists of a highly conjugated porphyrin skeleton (macrocycle) in which two hydrogen atoms are attached to two out of four nitrogen atoms sitting in the center of the molecule. The macrocycle is surrounded by four phenyl rings which are tilted out of the porphyrin plane. Figure 1.5 shows the optimized geometry of an isolated H$_2$TPP molecule as obtained from DFT by using a generalized gradient approximation [36] for exchange-correlation effects together with a density-of-states plot (b) and orbital pictures of the HOMO (c) and HOMO-1 (d). At the GGA-DFT level, the two highest occupied orbitals, the HOMO and HOMO-1, are separated by 0.4 eV followed by two closely spaced states at about 1 eV binding energy. The LUMO is separated from the HOMO by a GGA-DFT gap of about 1.7 eV. Focusing on the HOMO and HOMO-1, we observe distinct nodal patterns which should also be reflected in the respective momentum maps thereby allowing for a clear distinction of these two orbitals. For instance, the HOMO is both symmetric about the xz plane and about the yz plane, while the HOMO-1 is anti-symmetric about these two planes, i.e., exhibits nodal planes in the xz and yz planes.
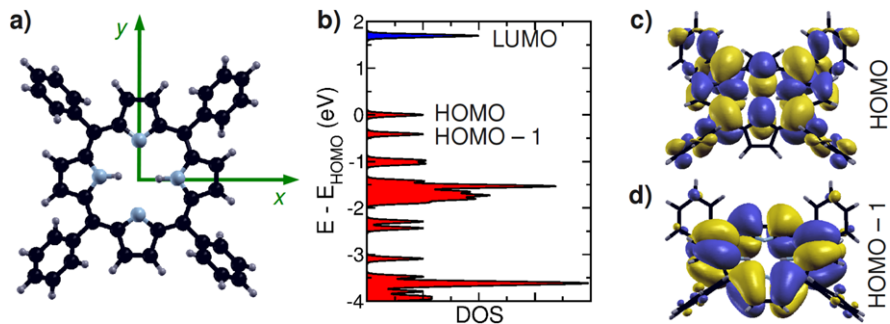
Fig. 1.5 (**a**) Chemical structure of tetraphenyl porphyrine with two hydrogen atoms saturating the bonds at the center of the molecule (H_2TPP). (**b**) Density of states of an isolated H_2TPP molecule as obtained from density-functional theory and a generalized gradient approximation for the exchange-correlation potential. (**c**) and (**d**) are corresponding orbital pictures of the HOMO and HOMO-1 separated by 0.4 eV
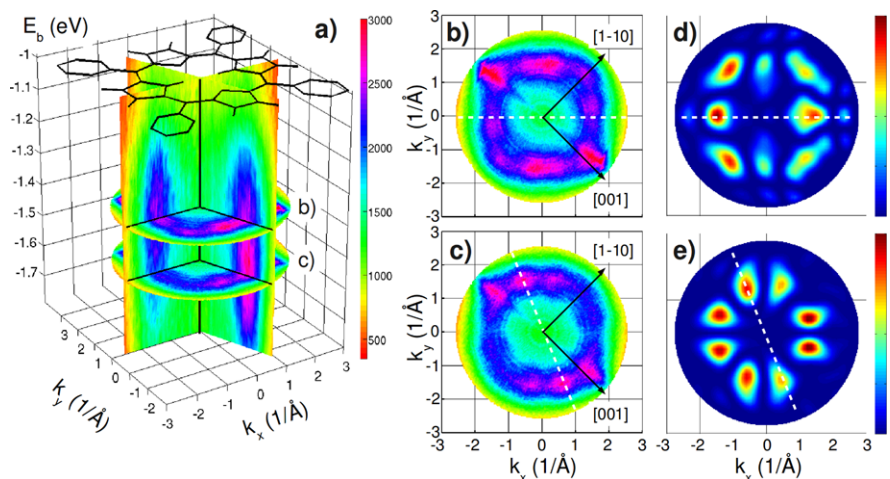

Fig. 1.6 (**a**) Experimental photoemission intensity (*color coded*) of a H_2TPP film as a function of binding energy E_b and momenta k_x and k_y, respectively. Two 'horizontal' sections at constant binding energies, -1.38 and -1.55 eV, as well as two 'vertical' sections at $k_y = 0$ and at an angle of $-22°$ from k_x are shown. Panels (**b**) and (**c**) display those constant binding energy momentum maps corresponding to $E_b = -1.38$ and -1.55 eV, respectively. Panels (**d**) and (**e**) are simulated momentum maps corresponding the H_2TPP HOMO and HOMO-1, respectively

In Fig. 1.6, ARPES data of a thin film of H_2TPP on Cu(110)-(2x1)O with a nominal thickness of 6 Å are compared to simulated momentum maps of the isolated molecule. By using 35 eV photons and the toroidal electron-energy analyzer at BESSY II, an energy window from about -1.0 to -1.8 eV below the Fermi level has been scanned. Further, by collecting electrons with a polar angle span from -70 to $+70°$ and by azimuthally rotating the sample around $180°$, a comprehensive data
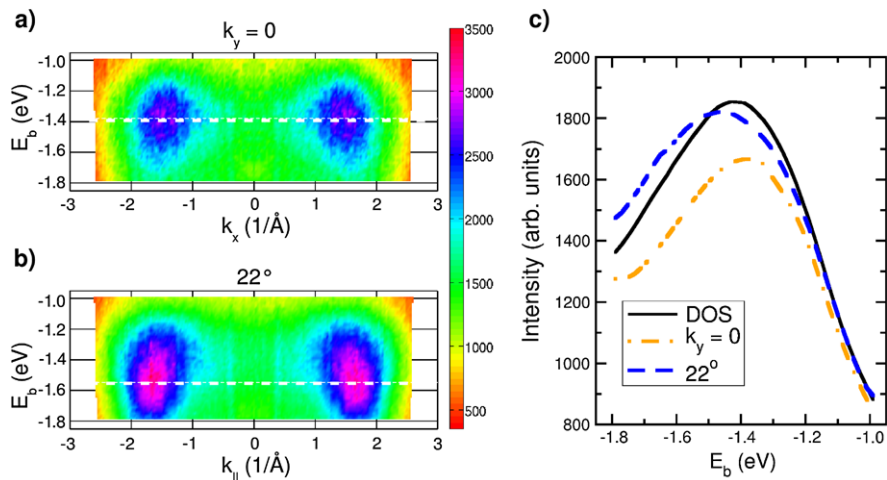
Fig. 1.7 (a) Band map of a H_2TPP film in the xz emission plane. (b) Same as (a) but for an emission plane rotated by $-22°$ with respect to the yz plane as indicated by the 'vertical' sections through the three-dimensional data cube shown in Fig. 1.6. (c) Energy-distribution curves (EDC) integrated over the whole k_x–k_y plane (*black line*) as well as for the emission planes shown in (b) and (c), respectively

set of the photoemission intensity, I, as a function of binding energy E_b and parallel momenta components k_x and k_y has been measured. These ARPES data are visualized in Fig. 1.6a in which the intensity is color-coded and several sections through the data are shown. On the one hand, two 'vertical' sections show the energy and polar angle distribution of the photocurrent for fixed azimuths of the emission plane. These tomographic sections are displayed separately in Fig. 1.7 and are discussed in more detail below. On the other hand, Fig. 1.6a also features two 'horizontal' sections at constant binding energies (CBE), namely at $E_b = -1.38$ and -1.55 eV. For clarity, these CBE momentum maps are also displayed in panels (b) and (c) of Fig. 1.6, respectively. Although quite close in energy, i.e., only 170 meV, the azimuthal intensity distribution appears different. While the map at -1.55 eV exhibits minima along the $k_x = 0$ and $k_y = 0$ directions, the intensity along these directions has clearly increased for the momentum map at -1.38 eV. This is indicative of the distinct symmetries and nodal patterns of the HOMO-1 and HOMO of H_2TPP mentioned earlier.

Indeed, the calculated momentum maps of the isolated molecule's HOMO and HOMO-1 displayed in panels (d) and (e) of Fig. 1.6 also reflect the orbitals' symmetry and their nodal patterns. In addition, also the (k_x, k_y) positions of the intensity maxima can be compared to the measured maps.[1] This comparison lets us conclude that the HOMO of the adsorbed H_2TPP is centered at an energy of -1.38 eV

---

[1]Note that the intensity maxima close to the substrate's [001] direction are due to a measurement artifact, i.e., a reflection of the primary photon beam into the detector.

whereas its HOMO-1 has a peak at a binding energy of -1.55 eV. It is also evident from the 'vertical' sections in Fig. 1.6a that the HOMO and HOMO-1 resonances are observed over several tenth of an eV and are, therefore, overlapping in energy. Hence, both momentum maps at -1.38 and -1.55 eV show contributions from both HOMO and HOMO-1 and the symmetry and nodal patterns cannot be seen as clearly as in the computed, pure maps. But how could we separate these two orbital resonances and assign to them the above mentioned binding energies?

The key are those 'vertical' sections through $I(E_b, k_x, k_y)$ which can be chosen in such a way as to highlight characteristic features of the respective molecular orbitals. For instance, the HOMO is expected to have maxima along k_x as indicated by the white dashed line in panel (b), while the HOMO-1 has a nodal plane in this direction. Therefore, ARPES scans along this azimuth project out contributions of the HOMO. Similarly, the HOMO-1 has intensity maxima for an emission plane rotated by 22° with respect to the k_y axis (dashed line in panel (c)), while the HOMO has almost vanishing intensity along this azimuth. Hence, this azimuth serves as a fingerprint for the HOMO-1. As can be seen from Fig. 1.6a, this allowed us to assign the energies of -1.38 eV and -1.55 eV to the center of the HOMO and HOMO-1 emissions and determine their energy width to be about 0.5 eV. For clarity, the ARPES band maps at the above mentioned azimuthal directions are also reproduced in Fig. 1.7. Panel (c) of this figure also shows the corresponding energy-distribution curves (EDC) integrated over all polar angles, i.e. parallel momentum values, along the k_x axis (red line) and the 22° azimuth with respect to the k_y axis (blue line). Also, these EDCs exhibit different energy peak positions allowing the HOMO and HOMO-1 to be separated. In contrast, an EDC integrated over the full polar and azimuthal angle dependence, i.e., integrated over the k_x–k_y plane (black line), yields a broad and featureless peak with no possibility to discern the contributions from the two involved orbitals. In summary, the characteristic (k_x, k_y)-dependences of molecular emissions allows their energy position and width to be determined beyond the limit of energy resolution. Our data also show that emission planes not carefully chosen may emphasize or suppress particular molecular orbitals due to selection rules inevitably involved in any photoemission process.

We conclude this section by discussing the azimuthal alignment of the H_2TPP molecules with respect to the Cu(110)-(2x1)O substrate. Tacitly, we have been assuming throughout this section that the molecule's (x, y) coordinate frame is rotated by 45° with respect to the principal substrate directions as already indicated in Fig. 1.6 and visualized more clearly in Fig. 1.8. Indeed, there is evidence for such an alignment from X-ray diffraction pole-figure measurements of 370 Å thick film of H_2TPP/Cu(110)-(2x1)O [35]. For these thicker films, the X-ray diffraction showed the $(5\overline{1}03)$ net plane of the triclinic H_2TPP polymorph crystal structure to be parallel to the substrate surface. In this plane, the porphyrin macrocycle is almost parallel to the substrate surface. Moreover, the epitaxial relationships revealed that the molecules are oriented such that the central hydrogens attached to the nitrogen atoms are pointing towards a 45° direction with respect to the [001] substrate axis [35] as also indicated in Fig. 1.8. In addition to this evidence derived from a 370 Å thick film, also the ARPES data for the 6 Å film reveal the identical alignment. As can be seen from Fig. 1.6, the chosen azimuthal orientation maximizes the
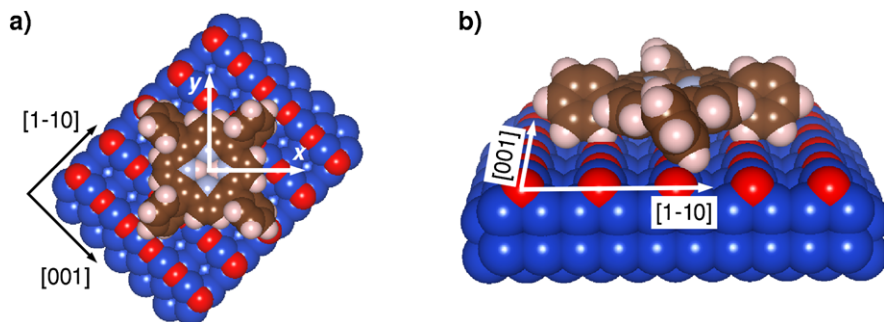
Fig. 1.8 Top (**a**) and side view (**b**) showing the azimuthal alignment of H_2TPP adsorbed on the Cu(110)-(2x1)O substrate. The substrate's [001], i.e., the oxygen row direction, and [1-10] directions are indicated as well as the (x, y) coordinate frame of the molecule which is rotated by 45° about the substrate's principal axes. Copper atoms are colored *dark blue*, oxygens *red*, carbons *dark brown*, nitrogens *light blue*, and hydrogens *light brown*

agreement with the calculated momentum maps for both the HOMO and HOMO-1. Thus, ARPES maps do not only allow molecular emissions to be identified but also enable azimuthal alignments of extremely thin films, down to monolayers, to be determined.

1.4.3 Reconstruction of Molecular Orbitals in Real Space

We continue by demonstrating the viability of the plane-wave approach for both reciprocal space mapping as well as real-space reconstructions of relatively complicated molecular orbitals. Here, we show that this approach allows reconstruction of the orbitals of para-sexiphenyl bonded to the Cu(110) surface. Not only are we able to reconstruct a real-space image of the HOMO but we also show that the PE intensity at the Fermi level that appears on adsorption has the orbital structure of the lowest unoccupied molecular orbital (LUMO).

When deposited on a Cu(110) substrate, sexiphenyl (6P) molecules align with their long molecular axes parallel to the [1-10] azimuth of Cu(110) [37], i.e., parallel to the copper rows and, upon saturation, form a well-ordered monolayer. A structural motif of this adlayer together with the underlying Cu(110) substrate is displayed in Fig. 1.9a. Here, we show the primitive surface unit cell of the saturated adlayer indicated by the blue arrows. This structure has been deduced from both low energy electron diffraction [38] and the STM in Fig. 1.9b. This typical room temperature STM image of a saturated monolayer of sexiphenyl on Cu(110) was obtained with a bias voltage 0.19 V.

In Fig. 1.9c, we show the angle-dependent photoemission of the sexiphenyl monolayer adsorbed on Cu(110) with the emission plane parallel to the long molecular axis. Comparison with equivalent photoemission data for the clean Cu(110) surface identifies the two features indicated by the red arrows as stemming from
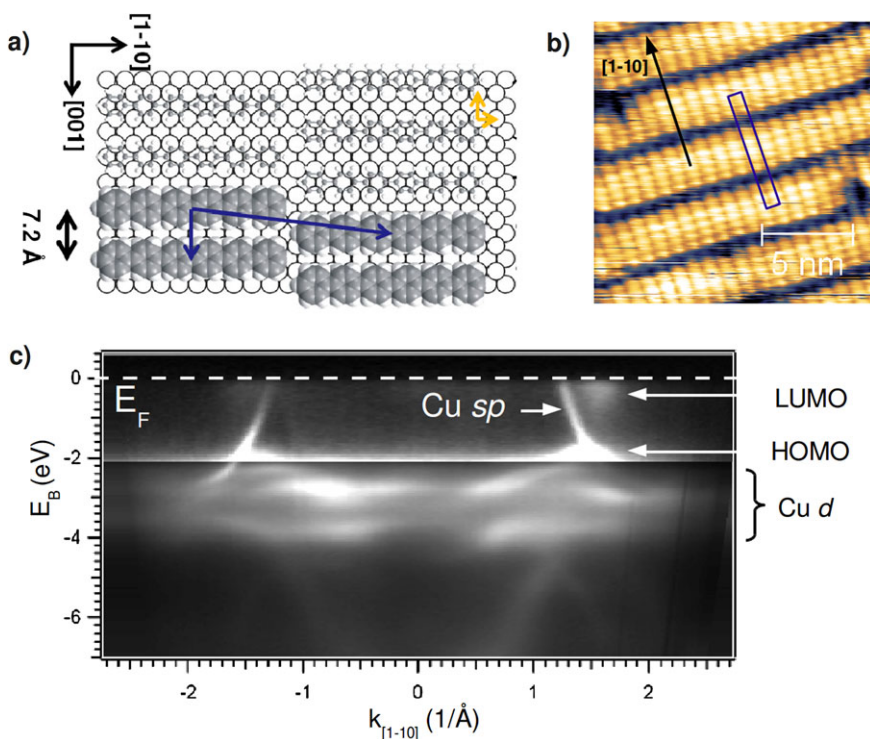
Fig. 1.9 (**a**) Schematic representation of the para-sexiphenyl (6P) monolayer on the Cu(110) surface. The long molecular axis is oriented parallel to the [1-10] direction of the Cu(110) surface, the primitive surface unit cell of the adlayer is indicated by *blue arrows*. (**b**) STM image of the 6P monolayer on the Cu(110) surface. The substrate [1-10] direction is indicated by the *arrow*, and the equivalent centered surface unit cell [c(2x22)] of the 6P adlayer is marked as the *blue rectangle*. (**c**) Angle-resolved photoemission intensity from the 6P monolayer on Cu(110) with an emission plane parallel to the long molecular axis. The *dashed line* indicates the Fermi level and *arrows* point at features that we identify as originating from the sexiphenyl HOMO and LUMO. Between 0 and −2 eV, the *intensity scale* has been magnified for clarity

molecule. The state slightly below the Fermi level is tentatively attributed to the partially filled LUMO, while the newly appearing emission with a binding energy of 1.9 eV is likely due to the sexiphenyl HOMO. The fact that the peaks are at positions in k_x direction which reflect the main spatial periodicity of the sexiphenyl HOMO [39] and LUMO, respectively, is already the first indication for this assignment.

A proof of this assignment can be given by measuring k_x–k_y momentum maps at the constant binding energies corresponding to these features appearing upon adsorption, i.e., at 0.3 and 1.9 eV below the Fermi level. Momentum maps at these two binding energies are shown in Fig. 1.10 and compared to the calculated FTs of the HOMO and LUMO from an isolated 6P molecule (Figs. 1.10c and d). The main characteristics, maxima at $k_x^{\mathrm{HOMO}} \approx \pm 1.45\,\text{Å}^{-1}$ reflecting the spatial periodicity set
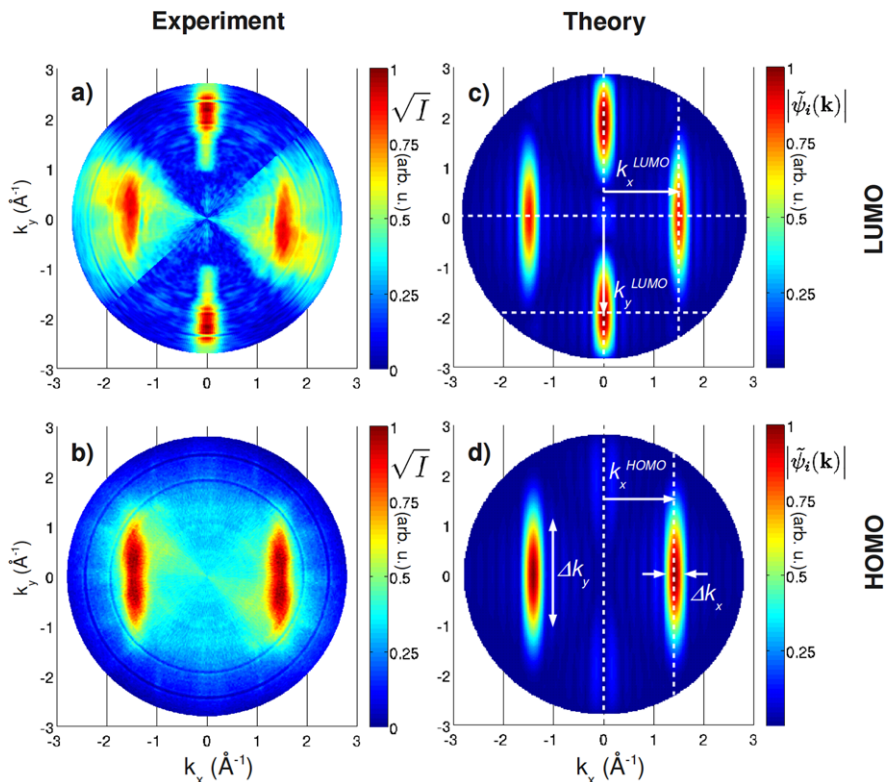
Fig. 1.10 Measured photoemission intensities (*left column*) compared to calculated Fourier transforms (*right column*). (**a**) Photoemission momentum map (square root of the intensity) from a 6P of sexiphenyl on Cu(110) at a binding energy of 0.3 eV corresponding to the 6P LUMO. (**b**) Same as in (**a**) but for a binding energy of 1.9 eV corresponding to the 6P HOMO. (**c**) Absolute value of the Fourier transform of the 6P LUMO calculated for an isolated molecule within DFT. (**d**) Same as in (**c**) but for the sexiphenyl HOMO. Characteristic features in the computed Fourier transforms are indicated by the *white arrows* as described in the text

by the length of one phenyl ring ($2\pi / k_x^{\mathrm{HOMO}} \approx 4.3$ Å) [39], are observed in the data as well as in the calculation. Also, the width Δk_x, which is inversely proportional to the length of the molecule, appears consistent in the PE data. The same holds for the extension in y direction, Δk_y, which is related to the width of a phenyl ring. We take these findings as strong evidence that the molecular feature observed at a binding energy of 1.9 eV can indeed be attributed to the sexiphenyl HOMO and, moreover, that its character is preserved even in a strongly interacting monolayer on a metal surface. In a similar manner, we are able to unambiguously assign the intensity close to the Fermi level to an emission from the filled LUMO (Fig. 1.10a and c). This emission thus indicates electron transfer from the metal into the former LUMO of the isolated molecule: as was the case for the HOMO, the nodal structure of the LUMO is found to be preserved on adsorption. Thus, we see that PE momentum
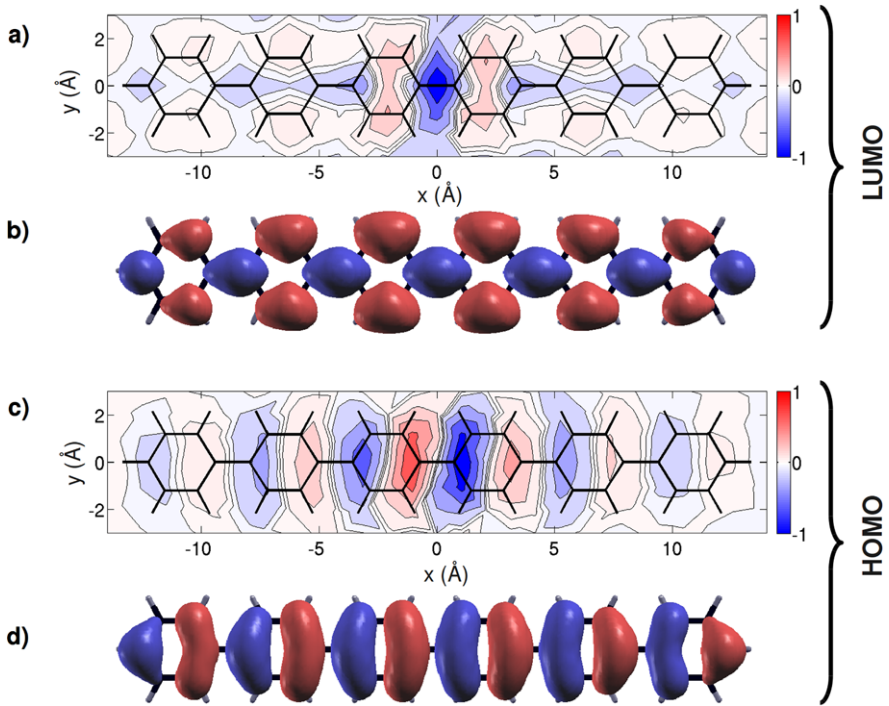
Fig. 1.11 Molecular orbitals reconstructed from photoemission data compared to DFT orbitals. (**a**) The 6P LUMO reconstructed from the PE momentum map at a binding energy of 0.3 eV. (**b**) LUMO of an isolated 6P molecule from DFT. (**c**) The HOMO of sexiphenyl reconstructed from the momentum map at a binding energy of 1.9 eV. (**d**) LUMO of an isolated 6P molecule from DFT. Experimentally determined orbitals are displayed as density plots where *red* (*blue*) *colors* indicate positive (negative) values isolines are added for clarity. The DFT orbitals are represented as isosurface plots using the same color code. The molecular backbone is indicated by *black lines*

maps provide fingerprints of molecular states allowing for their unique identification even in cases where there is a rather strong bonding interaction.

The ability to reproduce the PE momentum maps with Fourier transforms of the initial-state wave functions encouraged us to reconstruct real-space images of the molecular orbital densities from the experimental photoemission data. According to Eq. (1.2) we take the square root of the PE data and divide it by the polarization factor $|\mathbf{A} \cdot \mathbf{k}| \propto |\sin\theta \cos\chi - \cos\theta \sin\chi|$. Restricting the data to positive k_x values and considering the incidence angle $\chi = -40°$ of the p-polarized photons, this function has a maximum for a take-off angle $\theta = 50°$ and a minimum value of 0.64 at normal emission. Before performing the inverse FT of the processed PE data we mirror the data to the negative k_x plane and change their sign (or leave it unchanged) according to the parity of the wave function which is even (odd) for the HOMO (LUMO). By the latter procedure we restore phase information on the wave function to facilitate the comparison with calculated orbitals. The inverse Fourier transforms of the PE data for the adsorbed sexiphenyl HOMO and LUMO are compared with the DFT

calculated orbitals of the isolated molecule in Fig. 1.11. Spatial periodicities and nodal structure are well-conserved across theory and experiment. Because the resolution Δx in the reconstructed images is inversely proportional to the plane-wave cut-off $k_{\max}$ (thus $\Delta x = \pi / k_{\max}$), kinetic energies of around 30 eV as used in our experiments lead to $\Delta x \approx 1$ Å.

Compared to the DFT orbitals, both the HOMO and LUMO electron densities obtained from photoemission are more weighted around the center of the molecule, a distinction we tentatively attribute to the interaction with the Cu surface. Indeed, in sexiphenyl charge transfer salts the local distortions and the transferred electrons are located around the center of the molecule [40]. Furthermore, although STM images typically do not match molecular orbital images exactly, an STM image of a monolayer of sexiphenyl adsorbed on Cu(110) does show an electron density distribution that is weighted towards the center of the molecules (Fig. 1.9). Nonetheless, we feel that improvements in the PE signal-to-background ratio are necessary before any strong conclusions can be reached concerning the extent of orbital distortion introduced by the metal surface.

1.5 Conclusion

We have demonstrated that the simple relation between the photoemission intensity and the Fourier transform of the molecular orbital can be a valuable tool for the investigation of organic molecular films and their interfaces with metallic surfaces. We envision a wide applicability of the presented approach for studying the valence-band electronic structure of organic molecular films, particularly with the latest generation of angular-resolved display-type electron spectrometers. This may not only lead to a renaissance of angle-resolved photoemission spectroscopy in the field of organic electronics, but it also provides stringent tests for further development of accurate electronic-structure calculations.

References

1. N. Ueno, S. Kera, Prog. Surf. Sci. **83**, 490 (2008)
2. J. Repp, G. Meyer, S.M. Stojkovic, A. Gourdon, C. Joachim, Phys. Rev. Lett. **94**, 026803 (2005)
3. A. Kraft, R. Temirov, S.K.M. Henze, S. Soubatch, M. Rohlfing, F.S. Tautz, Phys. Rev. B **74**, 041402(R) (2006)

4. R. Temirov, S. Soubatch, A. Luican, F.S. Tautz, Nature **444**, 350 (2006). doi:10.1038/nature05270

5. J. Kröger, H. Jensen, R. Berndt, R. Rurali, N. Lorente, Chem. Phys. Lett. **438**, 249 (2007)

6. I. Torrente, K. Franke, J. Pascual, J. Phys. Condens. Matter **20**, 184001 (2008)

7. S. Soubatch, C. Weiss, R. Temirov, F. Tautz, Phys. Rev. Lett. **102**, 177405 (2009)

8. W.H.E. Schwarz, Angew. Chem., Int. Ed. Engl. **45**, 1508 (2006). doi:10.1002/anie.200501333

9. R. Temirov, S. Soubatch, O. Neucheva, A.C. Lassise, F.S. Tautz, New J. Phys. **10**, 053012 (2008). doi:10.1088/1367-2630/10/5/053012

10. S. Hüfner, *Photoelectron Spectroscopy* (Springer, Berlin, 2003)

11. S. Kera, S. Tanaka, H. Yamane, D. Yoshimura, K. Okudaira, K. Seki, N. Ueno, Chem. Phys. **325**, 113 (2006). doi:10.1016/j.chemphys.2005.10.023

12. P. Puschnig, S. Berkebile, A.J. Fleming, G. Koller, K. Emtsev, T. Seyller, J.D. Riley, C. Ambrosch-Draxl, F.P. Netzer, M.G. Ramsey, Science **326**, 702 (2009). doi:10.1126/science.1176105

13. F. Himpsel, J. Electron Spectrosc. Relat. Phenom. **183**, 114 (2011). doi:10.1016/j.elspec.2010.03.007

14. J. Ziroff, F. Forster, A. Schöll, P. Puschnig, F. Reinert, Phys. Rev. Lett. **104**(23), 233004 (2010). doi:10.1103/PhysRevLett.104.233004

15. J.E. Ortega, S. Speller, A.R. Bachmann, A. Mascaraque, E.G. Michel, A. Närmann, A. Mugarza, A. Rubio, F.J. Himpsel, Phys. Rev. Lett. **84**(26), 6110 (2000). doi:10.1103/PhysRevLett.84.6110

16. A. Damascelli, Phys. Scr. T **109**, 61 (2004)

17. P.J. Feibelman, D.E. Eastman, Phys. Rev. B **10**, 4932 (1974)

18. J.W. Gadzuk, Phys. Rev. B **10**, 5030 (1974). doi:10.1103/PhysRevB.10.5030

19. T. Permien, R. Engelhardt, C.A. Feldmann, E.E. Koch, Chem. Phys. Lett. **98**, 527 (1983)

20. N.V. Richardson, Chem. Phys. Lett. **102**, 390 (1983)

21. W.D. Grobman, Phys. Rev. B **17**, 4573 (1978). doi:10.1103/PhysRevB.17.4573

22. S.M. Goldberg, C.S. Fadley, S. Kono, Solid State Commun. **28**, 459 (1978)

23. E.L. Shirley, L.J. Terminello, A. Santoni, F.J. Himpsel, Phys. Rev. B **51**, 13614 (1995)

24. H. Daimon, F. Matsui, Prog. Surf. Sci. **81**, 367 (2006)

25. L. Broekman, A. Tadich, E. Huwald, J. Riley, R. Leckey, T. Seyller, K. Emtsev, L. Ley, J. Electron Spectrosc. Relat. Phenom. **144–147**, 1001 (2005). doi:10.1016/j.elspec.2005.01.022

26. N. Koch, A. Vollmer, I. Salzmann, B. Nickel, H. Weiss, J.P. Rabe, Phys. Rev. Lett. **96**, 156803 (2006). doi:10.1103/PhysRevLett.96.156803

27. H. Kakuta, T. Hirahara, I. Matsuda, T. Nagao, S. Hasegawa, N. Ueno, K. Sakamoto, Phys. Rev. Lett. **98**, 247601 (2007). doi:10.1103/PhysRevLett.98.247601

28. S. Berkebile, P. Puschnig, G. Koller, M. Oehzelt, F.P. Netzer, C. Ambrosch-Draxl, M.G. Ramsey, Phys. Rev. B **77**, 115312 (2008)

29. M.L. Tiago, J.E. Northrup, S.G. Louie, Phys. Rev. B **67**, 115212 (2003)

30. K. Hummer, C. Ambrosch-Draxl, Phys. Rev. B **72**, 205205 (2005)

31. D. Nabok, P. Puschnig, C. Ambrosch-Draxl, O. Werzer, R. Resel, D.M. Smilgies, Phys. Rev. B **76**, 235322 (2007). doi:10.1103/PhysRevB.76.235322

32. X. Gonze, J.M. Beuken, R. Caracas, F. Detraux, M. Fuchs, G.-M. Rignanese, L. Sindic, M. Verstraete, G. Zerah, F. Jollet, M. Torrent, A. Roy, M. Mikami, P. Ghosez, J.Y. Raty, D.C. Allan, Comput. Mater. Sci. **25**, 478 (2002)

33. M. Koini, T. Haber, O. Werzer, S. Berkebile, G. Koller, M. Oehzelt, M. Ramsey, R. Resel, Thin Solid Films **517**, 483 (2008). doi:10.1016/j.tsf.2008.06.053

34. C.C. Mattheus, A.B. Dros, J.B.A. Meetsma, J.L. de Boer, T.T.M. Palstra, Acta Crystalogr. C **57**, 939 (2001)

35. T. Djuric, T. Ules, S. Gusenleitner, N. Kayunkid, H. Plank, G. Hlawacek, C. Teichert, M. Brinkmann, M.G. Ramsey, R. Resel, Phys. Chem. Chem. Phys. (2011, submitted)

36. J.P. Perdew, K. Burke, M. Ernzerhof, Phys. Rev. Lett. **77**, 3865 (1996)

37. M. Oehzelt, L. Grill, S. Berkebile, G. Koller, F.P. Netzer, M.G. Ramsey, Chem. Phys. Chem. **8**, 1707 (2007). doi:10.1002/cphc.200700357

38. S. Berkebile, T. Ules, P. Puschnig, L. Romaner, G. Koller, A.J. Fleming, K. Emtsev, T. Seyller, C. Ambrosch-Draxl, F.P. Netzer, M.G. Ramsey, Phys. Chem. Chem. Phys. **13**, 3604 (2011). doi:10.1039/C0CP01458C
39. G. Koller, S. Berkebile, M. Oehzelt, P. Puschnig, C. Ambrosch-Draxl, F.P. Netzer, M.G. Ramsey, Science **317**, 351 (2007). doi:10.1126/science.1143239
40. M.G. Ramsey, M. Schatzmayr, S. Stafström, F.F.P. Netzer, Europhys. Lett. **28**, 85 (1994)